CAUSES OF INCREASED CORROSION AND HYDROGEN UPTAKE OF ZIRCALOY-2 CLADDING AT HIGH BURNUPS – A COMPARATIVE STUDY OF THE CHEMICAL COMPOSITION OF A 3 CYCLE AND A 9 CYCLE CLADDING

A. BARIS, S. ABOLHASSANI, R. GRABHERR, R. RESTANI
Nuclear Energy and Safety department, Paul Scherrer Institut,
CH-5232 Villigen PSI – Switzerland

R. SCHÄUBLIN
Department of Materials, ETH Zürich, Vladimir-Prelog-Weg, 8093 Zürich – Switzerland

Y.L. CHIU, H.E. EVANS
Metallurgy and Materials, Elms Rd, Birmingham B15 2SE – United Kingdom

K. AMMON
Kernkraftwerk Leibstadt AG, CH-5325 Leibstadt – Switzerland

M. LIMBÄCK
Westinghouse Electric Sweden AB, Västerås, S-721 63 – Sweden

ABSTRACT

This study concentrates on the oxidation and H-uptake which are among the important factors responsible for Zr based claddings' degradation during service. In depth characterization of a 3 and a 9 cycle rod by means of EPMA and ChemiSTEM is reported. The EPMA results show that the distribution of alloying elements is different in the case of the two materials at the metal-oxide interface. This suggests that the nature of the metal-oxide interfaces in the two samples is different. Increasing concentration of Fe and Ni is observed towards the outermost part of the oxide in both samples. Fe and Ni segregation is found before and after irradiation in all samples in the metal grain boundaries (GB). This could explain the enrichment of these alloying elements at the outer surface of the cladding. At high burnup Sn shows segregation in the metal GBs and the continuation of the same segregation to the oxide part of the metal-oxide interface is observed. The influence of these phenomena on the material's properties is discussed.

1. Introduction

The corrosion and hydrogen uptake of Zr alloys have recently been an intensive topic of research, mainly focusing on the causes of increased uptake in the reactor, to improve the safety issues. In this respect, several in reactor and autoclave studies have been reported recently. Many parameters have been explored as responsible factors for hydrogen pickup and its changes, including the diffusion through the oxide matrix [1], [2], [3]; the conductivity of the oxide layer [4], [5]; and the presence of pores in the oxide near the interface [6], [7], [8], [9], [10].

The distribution of alloying elements in the metal and oxide has a significant effect on the hydrogen pickup and oxidation properties of the material. It has been claimed that dissolution of certain alloying elements (such as Fe, Ni and Nb) in the oxide could change the diffusivity of H in the oxide layer by affecting the potential gradient through the oxide [2] or the mobility of interstitial protons [1], [11]. Both Fe^{3+} and Fe^{2+} dissolved in the oxide have been also associated with lower H-pickup [5], [12] and oxidation [12]. It must be noted that the role of iron on the H pickup has been claimed to be governed by its state: when in form of secondary phase particle (SPP) Fe is claimed to increase H pickup [13]. Regarding other elements, it has been shown as an example that significantly higher H diffusion rate is expected in Ni-containing oxides compared to oxides accommodating Fe or Cr [3].

It is known that the secondary phase particles (SPPs) are present in the alloy to enhance oxidation resistance [14]. Under irradiation they dissolve gradually and their solubility limit in the metal matrix is very low [15]. Therefore, their behaviour and redistribution in the metal matrix after dissolution could have a decisive effect on the further oxidation and H-uptake properties of the cladding. An Atom Probe Tomography (APT) study in un-irradiated Zr based alloys showed GB segregation of some elements in the metal [16]. In other studies Ni and Fe segregate in un-irradiated Zircaloy-2 both at the metal and the oxide grain boundaries [17], while Sn segregates in the oxide [18]. In respect to irradiated materials another APT study on the 9 cycle LK3/L material presented in the metal, Sn and Fe clustering in ring-shaped features suggesting <c>-loops and Fe and Cr rich nano-sized precipitates correlated to <a> loops, suggesting precipitation of these elements at the site of these loops or in their stress field.[19].

The evolution of the LK3/L cladding using 3, 5, 7 and 9 cycle samples has been reported in a previous study using techniques such as EPMA, TEM, SEM [20].The 3 and 9 cycle samples are further analysed by FIB tomography demonstrating that the volume fraction of cracks in oxide increases with the service time. [21]. The 9 cycle material showed the highest amount of cracks at the metal-oxide interface. Subsequently, the oxidation of the large hydride phases in the metal is claimed to enhance crack formation at late life of the cladding [10].

In this study the chemical composition of two irradiated LK3/L Zircaloy-2 samples (the 3 and 9 cycle cladding) are compared using EPMA for sub-micrometric and ChemiSTEM for nanometric scale analysis. Here the aim has been:

a- to examine the dissolution phenomena for all alloying elements in the oxide and the metal, by means of both techniques, and
b- b- furthermore by means of the nanometric compositional analysis in STEM try to trace these elements both in the matrix and at grain boundaries.
c- Attempt to search for differences between the two materials and correlate those differences to the change of H uptake at high burnups.

2. Materials and Methods

2.1. Materials

Zircaloy-2 samples with LK3/L grade have been studied. The cladding is designed by Westinghouse Electric [22]. The samples served in the Swiss KKL (Kernkraftwerk Leibstadt) boiling water reactor (BWR). The composition of the LK3/L material and heat treatment parameters are provided in Table 1. The cumulative annealing parameter (A) specifies the heat treatment and is described in references [23], [24].This study compares a 3 and a 9 cycle[1] sample. The weight gain and hydrogen pick-up (HPU) data of these claddings have been already measured by Abolhassani et al. [25]. An un-irradiated material from the same batch has been added to the samples examined by TEM in order to observe the material before irradiation. In Table 2 the important parameters of the claddings are summarized. For hydrogen measurements the inert-gas fusion method using an instrument supplied by LECO was employed, in this study total hydrogen content is reported, whereas PSI also provides separately

LK3/L composition	Sn	Fe	Cr	Ni	Fe+Cr+Ni	O (ppm)	Si (ppm)	log A
wt%	1.34	0.18	0.11	0.05	0.34	1320	70	-14.2
at%	1.02	0.29	0.19	0.077	0.557			

Table 1 The nominal composition of the LK3/L fuel rod with Zr in balance [25].

[1] Each cycle is 11 months and the reactor is down for service for approximately one month per year [17].

Residence time (cycle)	Segment elevation (mm)	Local burnup (MWd/kgU)	Average oxide thickness (µm)	Total hydrogen content (ppm)	Rod average burnup (MWd/kgU)
3	2011	41	4.4 (±0.7)	44	36
9	2039	89	46 (±2.5)	595	78.7

Table 2 Parameters of the LK3/L materials investigated in this study [25].

the H content in the metal and in the oxide [26]. More information regarding the water chemistry and irradiation scheme can be found in reference [27].

2.2. Sample preparation

The TEM samples have been prepared by FIB using a Zeiss NVision 40 system in the case of the irradiated materials, and by electrochemical polishing in the case of the un-irradiated material for which only a metallic sample was observed. For more details of electro-polishing please refer to [24]. Details of sample preparation for the EPMA measurements are provided in [10]. In the case of the 3 cycle EPMA results the sample was prepared slightly differently.

2.3. Characterization Techniques

Electron Probe Microanalysis (EPMA)

The Electron Probe Microanalysis (EPMA) was performed using a JEOL JXA-8500F EPMA with field emission gun (FEG). All measurements were obtained using the K_α signal of O, Cr, Ni, Fe, and L_α signal of Zr and Sn. In reference [10] the details of detections limits are described. Point measurements have been carried out using the smallest beam size at 15 kV acceleration voltage. The spatial resolution of the elemental maps is 200-300 nm. Beam current between 240-260 nA was used during all elemental maps and point scans. Quantitative point analyses were performed in the metal and in the oxide. The maps are only qualitative and represent the distribution of the elements. Therefore, it is worth mentioning that different maps cannot be compared on a quantitative basis.

ScanningTransmission Electron Microscopy (STEM)

The TEM samples were investigated using an FEI TALOS F200X (FEG) TEM equipped with ChemiSTEM for high resolution chemical analysis. This instrument is equipped with 4 EDX detectors in order to achieve high speed analytical measurements. During the study 200kV acceleration voltage was applied. Element maps and chemical point analysis for Zr, O, Fe, Cr, Ni, and Sn were produced at different positions in the samples. During the quantifications K_α peaks of O, Cr, Ni, Fe, and L_α peaks of Zr and Sn have been taken into account.

3. Results

3.1. EPMA results

3 cycle sample

The result of a quantitative point line-scan through the metal-oxide interface is shown in Figure 1. Cr shows the largest scatter which can be explained by the higher number of SPPs in the material, therefore during the line-scan the beam can hit many Cr containing SPPs.

	3 cycle LK3/L	9 cycle LK3/L	Un-irradiated LK3/L
Metal		X	X
Metal-oxide interface	X	X	
Outer part of the oxide	X*	X	

Table 3 The investigated areas on the different samples. *Part of metal-oxide interface sample (i.e. full oxide has been studied).

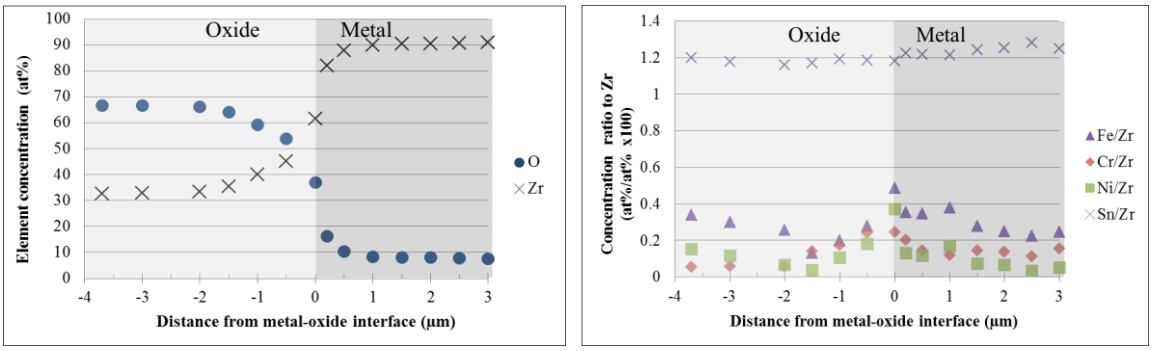

Figure 1 EPMA point line-scan through the metal-oxide interface of the 3 cycle sample. Left: Zr and O, right: alloying elements.

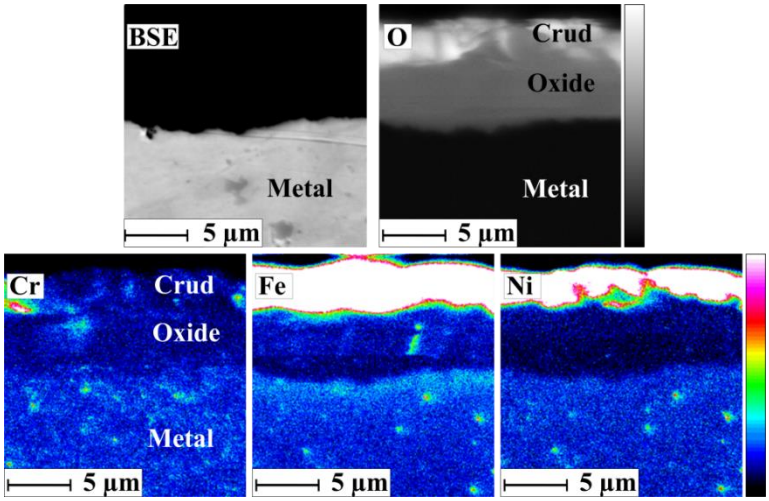

Figure 2 BSE micrograph and EPMA elemental maps of the metal-oxide and oxide-crud interface of the 3 cycle sample. The change in colour between the metal and the oxide is due to the change in the phases, qualitative point measurements (Figure 1) are used when comparing the concentration of the phases.

It is reminded that not all of these SPPs contain Fe which is already dissolved from most of the $Zr(Fe, Cr)_2$ SPPs as it can be observed on the maps. In Figure 2 EPMA maps of O, Cr, Fe, and Ni are presented through the crud-oxide and oxide-metal interfaces. SPPs still exist in the metal however the dissolution is already detected. Both Figure 1 and Figure 2 suggest that an iron rich region builds up in the metal close to the metal-oxide interface. Furthermore, the oxide at the interface is depleted of the alloying elements. Further studies have confirmed (not shown here) that this is a general behaviour of the alloying elements at this stage of irradiation. The concentrations of the metal and oxide matrices are given in Table 4.

9 cycle sample

For the detailed characterization of the 9 cycle sample by EPMA and other methods please refer to [10]. In that study it has been shown that after 9 cycles the SPPs are mainly dissolved and some remnants of the $Zr(Fe, Cr)_2$ are revealed containing Cr but no or very little amount of Fe. In this study brief examples are given for the ease of comparison. The studies of the metal-oxide interface of this 9 cycle segment have revealed that Fe and Ni have both a different behaviour at the metal-oxide interface in comparison to the behaviour of the 3 cycle sample. Figure 3 and Figure 4 present the chemical analysis and the elemental maps of the metal-oxide interface of the 9 cycle cladding. Detailed analysis of these regions have not shown accumulation of any alloying element at the metal-oxide interface, in the metal side and the transition of these elements through the interface has shown to be continuous and the concentrations are similar at the oxide and metal parts in the close environment of the interface [10]. On the line-scan the concentration values of Cr have large scatter in the case

Phase	O (at%)	Zr (at%)	Sn (at%)	Cr* (at%)	Fe* (at%)	Ni* (at%)
Oxide	65.56	33.88	0.43	0.035	0.08	0.012
Metal	7.84	90.49	1.15	0.21	0.25	0.05

Table 4 Average concentrations of the oxide and the metal matrix by EPMA, 3 cycle sample.
* For the alloying element concentration in the matrix please refer to the TEM result.

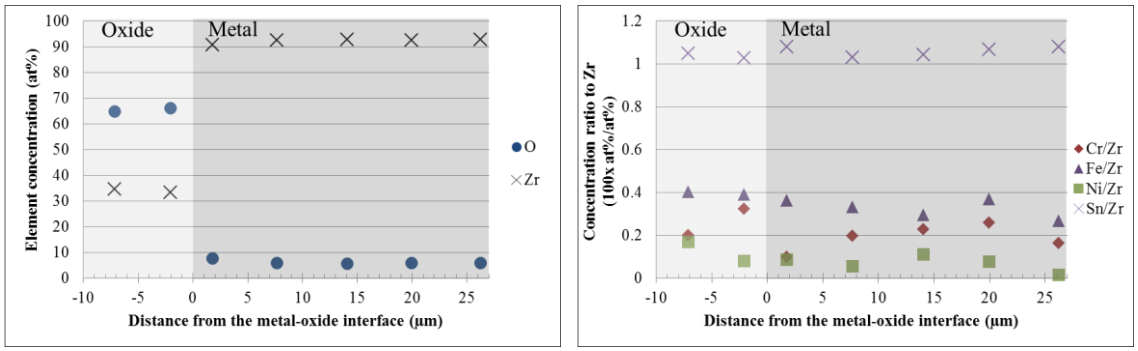

Figure 3 EPMA point line-scan through the metal-oxide interface of the 9 cycle sample. The measurement shows the oxide close to the interface. Left: Zr and O, right: alloying elements. For the measurements on the entire thickness of the oxide please refer to [10].

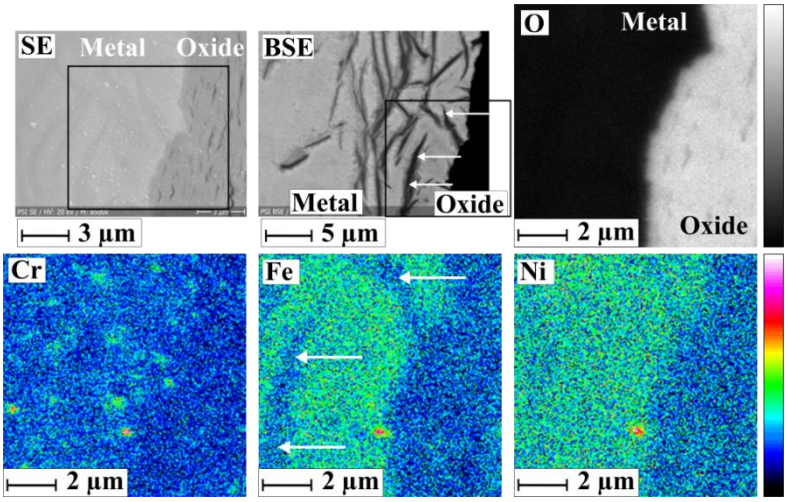

Figure 4 SE, BSE micrographs and EPMA elemental maps at the metal-oxide interface of the 9 cycle sample. White arrows indicate hydrides. The change in colour between the metal and the oxide is due to the change in the phases, qualitative point measurements (Figure 3) are used when comparing the concentration of the phases.

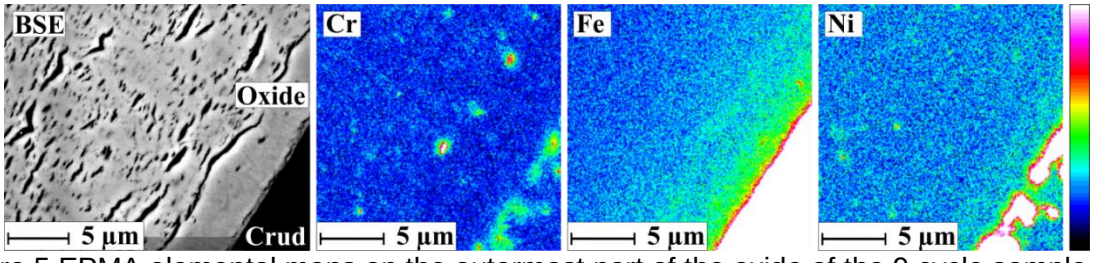

Figure 5 EPMA elemental maps on the outermost part of the oxide of the 9 cycle sample.

Phase	O (at%)	Zr (at%)	Sn (at%)	Cr* (at%)	Fe* (at%)	Ni* (at%)
Oxide	65.72	33.67	0.34	0.06	0.14	0.026
Metal	6.19	92.29	0.98	0.17	0.30	0.06

Table 5 Average concentrations of the oxide and the metal matrix by EPMA, 9 cycle sample.
* For the alloying element concentration in the matrix please refer to the TEM result.

of this material as well; due to the remnants of SPPs. For more detailed characterization and comparison of the microstructure of the metal-oxide interface and the micro-crack structure of the two samples please refer to [21]. Figure 4 reveals that the hydrides in the metal are depleted in Fe, and measurements have shown depletion of Ni as well. This point will be further discussed in section 3.2. EPMA maps and point measurements have shown that increasing Fe and Ni content is present towards the surface of the cladding. One example is shown in Figure 5. The concentrations of the metal and oxide matrices are given in Table 5.

3.2. TEM results

Un-irradiated sample

In order to observe the material before irradiation, ChemiSTEM measurements have been carried out on an electro-polished archive material. The two types of SPPs have been revealed (not shown here). The average composition of the metal matrix and the highest measured composition for the two types of SPPs are shown in Table 6. The high oxygen signal possibly originates from the natural oxide film that has formed on the thin foil. These SPP concentration values do not represent the highest compositions expected (i.e. the atomic concentrations for each species of the SPPs). In Figure 6 the grain boundary segregation of Fe and Ni prior to irradiation is shown.

3 cycle sample

After 3 years in reactor the SPPs have dissolved to certain extent (Table 7) and the segregation of Fe and Ni at the metal GBs are observed as it is shown in Figure 7. Figure 8 shows a dissolving SPP in the oxide close to the metal-oxide interface. Fe and Ni segregation in some oxide GBs is observable. Very low O concentration is measured in the oxide matrix, thus sub-stoichiometric oxide is assumed. For more quantitative data regarding oxygen please refer to the EPMA results. As the lamella was prepared at the metal-oxide interface high Fe concentration is measured in the metal due to the Fe-enrichment of this region (Figure 1 and Figure 2). This value does not represent the Fe concentration in the bulk matrix; for that please refer to Table 4.

Phase	O (at%)	Zr (at%)	Sn (at%)	Cr (at%)	Fe (at%)	Ni (at%)
Metal matrix	18.51	80.42	0.95	0.008	0.10	0.007
$Zr_2(Fe, Ni)$	5.86	72.89	0.28	0.11	12.44	8.42
$Zr(Fe, Cr)_2$	7.90	64.74	0.52	13.01	13.66	0.17

Table 6 The measured average metal matrix composition from 3 points in the un-irradiated LK3/L. Composition of the SPPs: the highest measured concentration is given.

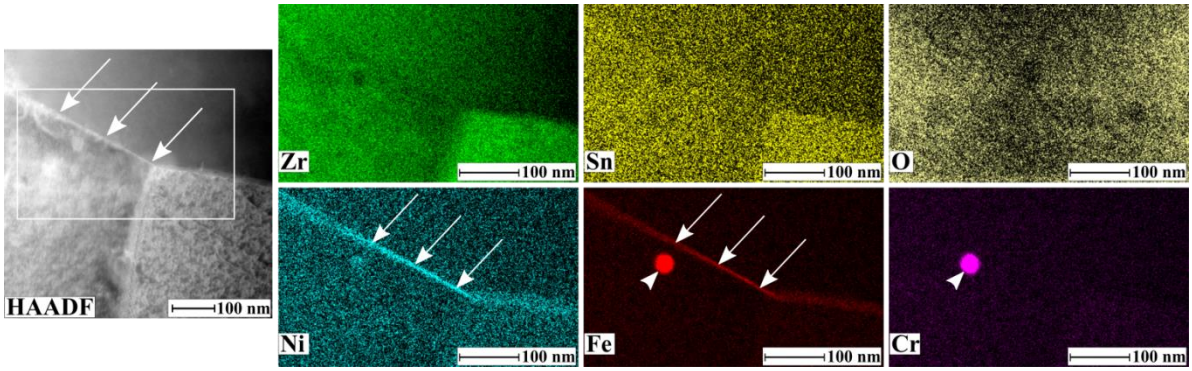

Figure 6 HAADF image and ChemiSTEM maps on the un-irradiated LK3/L sample. The mapped area is marked by the white rectangle. GB segregation of Ni and Fe is marked by arrows. A $Zr(Fe,Cr)_2$ SPP is marked by the arrowhead.

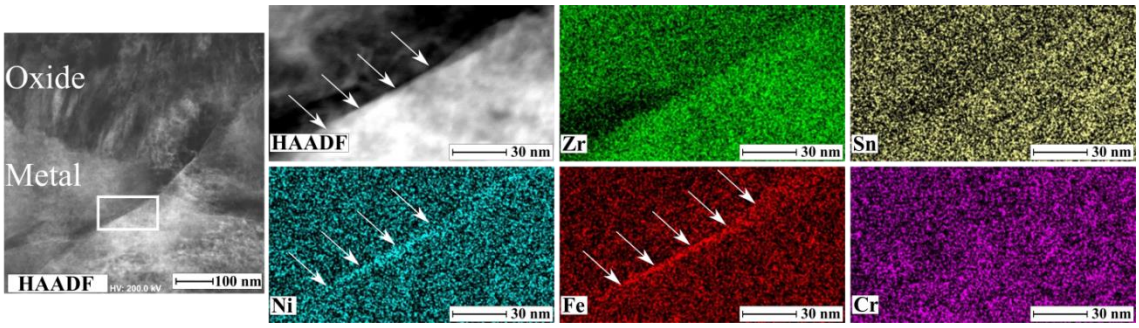

Figure 7 HAADF image and ChemiSTEM maps of a metal GB close to the metal-oxide interface in the 3 cycle sample. The mapped area is marked by the white rectangle. GB segregation of Ni and Fe is marked by arrows.

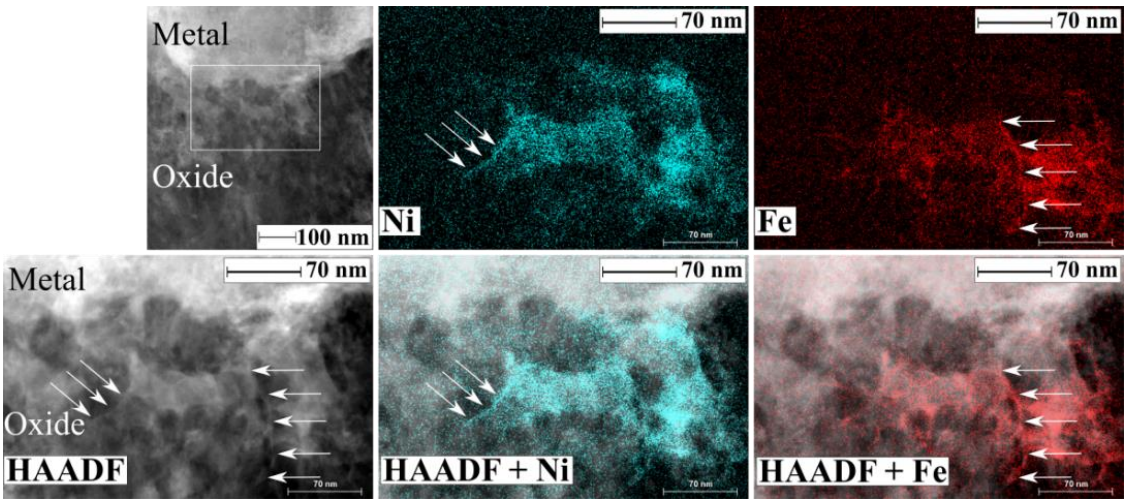

Figure 8 HAADF image and ChemiSTEM maps on the oxide close to the metal-oxide interface of the 3 cycle sample. The mapped area is marked by the white rectangle. Arrows indicate fine lines of Fe and Ni.

Phase	O (at%)	Zr (at%)	Sn (at%)	Cr (at%)	Fe (at%)	Ni (at%)
Metal matrix*	15.62	82.52	1.07	0.04	0.67	0.068
Fe-Ni SPP in metal**	14.46	80.92	0.90	0.086	2.18	1.45
Fe-Cr SPP in metal	14.98	80.14	1.06	2.82	0.82	0.17
Oxide matrix*	49.24	49.70	0.74	0.015	0.24	0.06
Fe-Ni SPP in oxide	46.40	45.52	0.32	1.41	4.59	2.75
Fe-Cr SPP in oxide	43.89	43.38	0.71	10.20	1.46	0.35

Table 7 Results of point analysis by ChemiSTEM. Average metal and oxide matrix composition from 3 points measured at the metal-oxide interface of the 3 cycle cladding. Composition of the SPPs in both phases: the highest measured concentration is given. * For the O and Zr content of the metal and oxide matrix please refer to the EPMA result. **Measurements based on spectra collected during mapping, i.e. providing only semi-quantitative data.

9 cycle sample

The ChemiSTEM results revealed that at high burnup not only Fe and Ni but also Sn segregate at the GBs (Figure 9). Segregation of Sn has been observed after 7 cycles as well (not shown here). Cr shows slight segregation in the GBs of the metal. The composition of the metal matrix has been measured by point analysis collected in the metal 2.5-7 µm from the interface (Table 8). Line-scan through the metal-oxide interface (not shown here) has revealed this oxide is stoichiometric both away from the interface as well as in the vicinity of the interface; thus very thin (~5-10 nm) transition layer is observed, i.e. the O signal drops

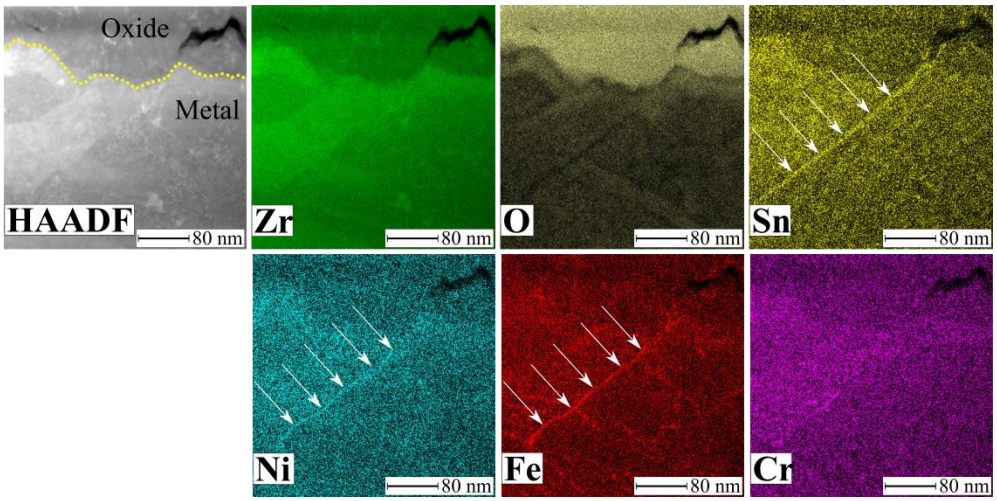

Figure 9 STEM micrograph and ChemiSTEM EDX maps at the metal-oxide interface of the 9 cycle sample. The arrows show the GB segregation. The yellow dashed line on the HAADF image represents the metal-oxide interface.

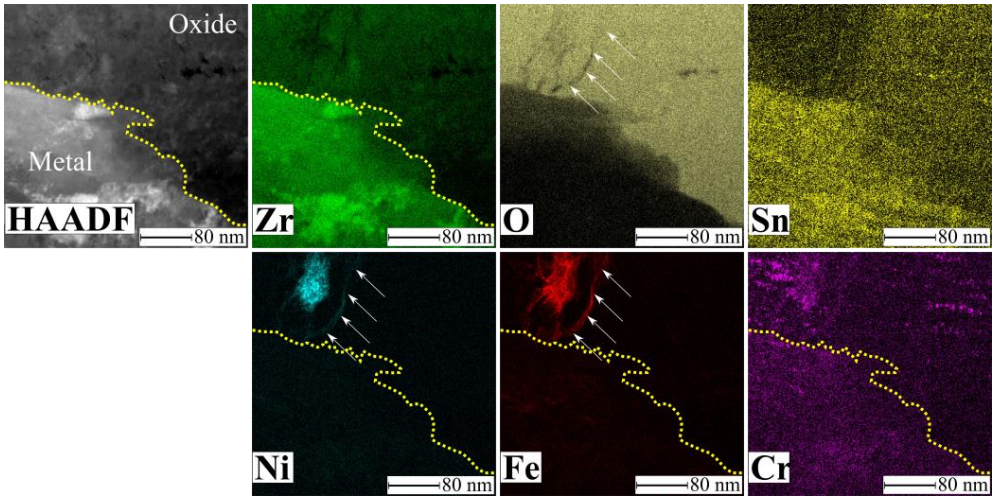

Figure 10 STEM micrograph and ChemiSTEM maps at the metal-oxide interface of the 9 cycle sample. A remnant of a Zr_2(Fe, Ni) SPP is revealed in the oxide. Arrows show Fe and Ni segregation in the shape of a fine line in the oxide part. The yellow dashed lines represent the metal-oxide interface.

suddenly at the interface. A remnant of an SPP in the oxide close to the metal-oxide interface is shown in Figure 10. The maps show that Fe and Ni segregate in the oxide in the shape of a fine line away from the core of the SPP, presumably in an oxide GB.

Another aspect which should be taken into account at higher burnups is the hydride formation in the metal matrix. The 9 cycle cladding showed 595 ppm H at the same elevation where the TEM sample has been prepared. This amount is highly above the solubility limit of H in Zr or Zircaloy-2 even at the service temperature. This suggests that most of the H was present as precipitated hydride phases even during the service. It has been shown that these phases are large objects and they have a deleterious effect on the hydrogen uptake and oxidation [10]. Point analyses in the metal matrix and the hydrides confirmed that hydrides systematically contain 1.2 times less Fe, and Ni and 1.7 times less Sn than that measured in the metal. The ChemiSTEM maps on the hydrides confirm this observation, shown in Figure 11. In the case of Cr, despite a certain drop observed on the images, clear depletion was difficult to detect in the hydrides.

Phase	O (at%)	Zr (at%)	Sn (at%)	Cr (at%)	Fe (at%)	Ni (at%)
Metal matrix*	24.41	74.12	1.01	0.03	0.36	0.07
Fe-Ni SPP in metal**	23.85	64.52	0.095	0.66	3.14	5.72
Fe-Cr SPP in metal	14.74	74.94	0.76	8.65	0.84	0.075
Oxide matrix***	66.96	32.50	0.30	0.03	0.18	0.028
Fe-Ni SPP in oxide	65.48	26.81	0.05	0.31	3.29	4.06
Fe-Cr SPP in oxide	74.035	21.87	0.22	3.01	0.84	0.02

Table 8 The average metal and oxide matrix composition each from 3 points; 9 cycle cladding. Composition of the SPPs in both phases: the highest measured concentration is given. For the O and Zr content of the metal and oxide matrix please refer to the EPMA result. *Data collected 2.5-7 µm away from the interface. **Measurements are based on spectra collected during mapping, i.e. providing only semi-quantitative data. ***Measured at the outer part of the oxide.

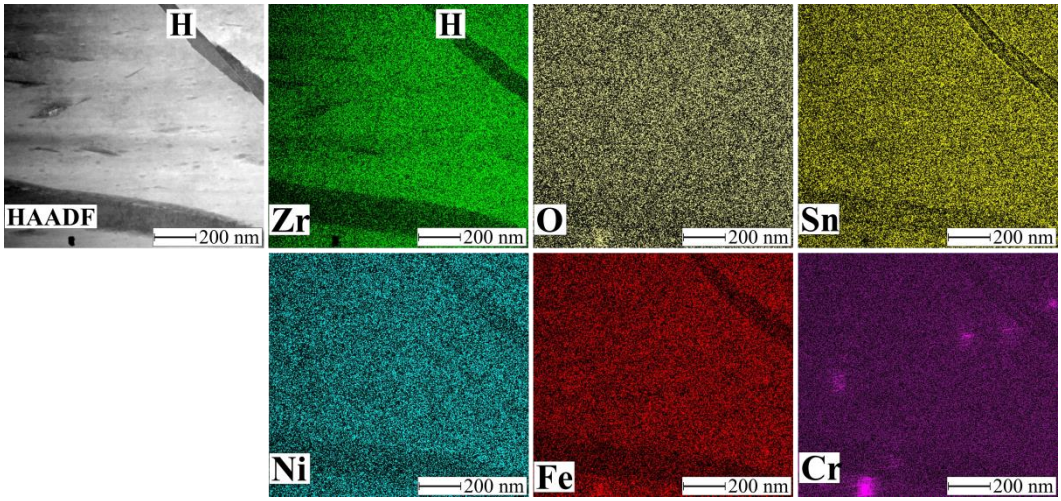

Figure 11 HAADF micrograph and ChemiSTEM maps on the hydrides in the metal; 9 cycle sample. H: Hydrides.

4. Discussion

The aim of this study has been to explore in depth the chemical changes occurring in the cladding after two different stages of lifetime. These chemical changes are then expected to reveal the causes of change of behaviour and in particular of increased hydrogen uptake at higher burnups. Independent of limitations of the techniques used (e.g. the difficulties inherent to oxygen quantification, or the spatial resolution of different techniques, etc.) results point to specific trends. Certain observations have been previously reported, and the present studies, provide further confirmation of the previous observations. As an example, continuous dissolution of alloying elements or build-up of hydrides as a function of time is well established. Other observations are not regularly observed in the literature, and add to the panoply of parameters to be considered in the search for the causes of increased hydrogen uptake at high burnup. As an example, the redistribution of alloying element around the hydrides, and their depletion from alloying elements will influence the hydrogen uptake. The fact that the hydrides repel alloying elements will lead after long-term irradiation where the matrix is rich in alloying elements to the growth of the existing hydrides rather than nucleation and growth of smaller grains. This phenomenon could be at the origin of accumulation of hydrides at the outer wall of the cladding, and add an extra parameter to the stresses developed in the material.

Grain boundary segregation is another phenomenon which is possible to reveal with new tools in the TEM. Recently atom probe and TEM can reveal to greater extent these segregations. However, the segregation observed in archive material is expected to disappear with irradiation: assuming in the same manner as the SPPs, the GB segregation to “dissolve”, under irradiation. However, the 3, 7 (not shown here) and 9 cycle studies, reveal

persistent presence of such segregation. This would indicate that the GB segregation is a path for the diffusion. It could be considered rather than “segregation”; as a “highway” for the different alloying elements to diffuse out of the metal matrix, due to their low solid solubility limit.

On the other hand EPMA studies systematically showed increasing concentrations of Fe towards the outer surface of the oxide both in 3 and 9 cycle materials. We can conclude that this is a general behaviour of Fe in zirconia. Fe seems to dissolve with a higher rate in the metal and the oxide and diffuse to the free surface. This phenomenon occurs without irradiation as well [28]. Here a brief reference to the crud can be made, despite the fact that crud has not been the topic of the current research. Both in reactor and in autoclave, this Fe migration to free surface could influence the crud formation, or in turn the crud could change the behaviour of Fe in the oxide.

The presence of dissolved Fe^{3+} in the oxide scale is claimed as responsible parameter for lowering the H-pickup [12]. The 3+ state is reported as most common in the outer part of the oxide on Zircaloy-4 [12]. The oxidation state of the dissolved Fe has not been examined in this current study; however the Fe-rich outer oxide layer is observable in both samples. As it is reported, the 3 cycle sample shows lower HPU than the 9 cycle. Several factors are responsible for this difference and one factor could be the protectiveness or chemical composition of the outermost oxide layer. However, we conclude that the protection of this layer is negligible after a certain period, namely once there is an interconnected pore system which allows the water flow inside the oxide.

Similar observation in the case of Ni is presented. However, Ni is claimed to have a negative effect on the H-pickup by enhancing the diffusion of H through the oxide [3].

5. Conclusion

The comparison of the chemical changes present at the metal-oxide interface of a medium burnup (3 cycle) and very high burnup (9 cycle) fuel cladding with the same grade of Zircaloy-2 (LK3/L) reveals clear differences between the nature of the two interfaces. The following findings can be reported:

The dissolution rate in the metal side of the interface is clearly much less in the 3 cycle cladding. Furthermore, the presence of large hydrides in the 9 cycle material, which clearly repel the alloying elements, enriches further the surrounding metal matrix in the case of high burnup material, with different dissolved alloying elements.

In the oxide, two significant differences can be seen: the oxide matrix of the 3 cycle cladding shows oxygen sub-stoichiometry, which cannot be revealed in the high burnup oxide. Furthermore, the concentration of alloying elements on the two sides of the interface, in 3 cycle cladding show an accumulation of alloying elements at the metal-side of the interface, which is not present in the case of the 9 cycle oxide. These observations confirm the fact that the higher burnup oxide will have a higher HPU due to lower conductivity of the stoichiometric zirconia.

In both claddings metal grain boundary segregation is observed. It is however interesting to note that Sn is present only in the high burnup cladding and can also be slightly observed in the oxide close to the interface. Although the segregation of Sn is surprising due to its solid solubility, such segregation in the oxide is claimed to degrade the oxidation properties by helping the tetragonal to monoclinic transformation [29]. Therefore the irradiation induced segregation of Sn at the GBs could increase the HPU at high burnups.

With a great coincidence, in both materials, one Zr_2(Fe,Ni) SPP is observed in the TEM in the vicinity of the interface in the oxide. Both precipitates show early stage of their oxidation, and alloying elements in the surrounding of the SPPs which seem to decorate the oxide grain boundary. These clusters are formed a few nm away from the core of the observed SPPs.

This could mean that these elements use GBs as paths for diffusion, at the early stage of incorporation into the oxide.

Acknowledgements

The authors would like to acknowledge Mr. A. Bullemer for his support with the EPMA sample preparation at PSI and Mr. J. Tian for his assistance on ChemiSTEM at the University of Birmingham. This research project is supported by swissnuclear and the authors acknowledge their financial support. Westinghouse Electric Co. and Kernkraftwerk Leibstadt are acknowledged for providing the investigated materials. This research team is a partner of MUZIC-3 international collaboration.

References

[1] K. Une, K. Sakamoto, J. Matsunaga, Y. Etoh, M. Aomi, I. Takagi, K. Sawada and H. Watanabe, “Controlling Factors in Hydrogen Absorption of Zirconium Alloys,” in *Proceedings of TopFuel 2012,*, Manchester, UK, 2012.

[2] K. Kakiuchi, N. Itagaki, T. Furuya, A. Miyazaki, Y. Ishii, S. Suzuki, T. Terai and M. Yamawaki, “Role of iron for hydrogen absorption mechanism in zirconium alloys,” *Zirconium in the Nuclear Industry: Fourteenth International Symposium,* pp. 349-366, 2005.

[3] K. Takahashi, T. Iwasaki and M. Inagaki, “Effects of additive elements and precipitate behavior in oxide films on hydrogen pick-up of zirconium alloys,” in *LWR fuel performance meeting*, 2014.

[4] K. Baur, F. Garzarolli, H. Ruhmann and H. J. Sell, “Electrochemical examinations in 350 C water with respect to the mechanism of corrosion-hydrogen pickup,” *Zirconium in the Nuclear Industry: Twelfth International Symposium,* pp. 836-852, 2000.

[5] A. Couet, A. Motta, A. Ambard and R. Comstock, “Hydrogen pickup mechanism in zirconium alloys,” *Zirconium in the Nuclear Industry: 18th International Symposium,* pp. 312-349, 2018.

[6] M. B. Elmoselhi, B. D. Warr and S. McIntyre, “A study of the hydrogen uptake mechanism in zirconium alloys,” *Zirconium in the Nuclear Industry: Tenth International Symposium,* pp. 62-79, 1994.

[7] D. Khatamian, “Diffusion of Hydrogen in the Oxides of Annealed Zr-1Nb, Zr-2.5Nb and Zr-20Nb Alloys,” *Atomic Energy of Canada Ltd.(AECL), Report No. RC-843-92-138,* 1992.

[8] B. Cox and Y. M. Wong, “A hydrogen uptake micro-mechanism for Zr alloys,” *Journal of Nuclear Materials,* vol. 270, no. 1-2, pp. 134-146, 1999.

[9] N. Ramasubramanian, V. Perovic and M. Leger, “Hydrogen Transport in the Oxide and Hydrogen Pickup by the Metal During Out-and In-Reactor Corrosion of Zr-2.5 Nb Pressure Tube Material,” *Zirconium in the Nuclear Industry: Twelfth International Symposium,* pp. 853-876, 2000.

[10] A. Baris, R. Restani, R. Grabherr, Y. L. Chiu, H. E. Evans, K. Ammon, M. Limbäck and S. Abolhassani, “Chemical and Microstructural Characterization of a 9 Cycle Zircaloy-2 Cladding using EPMA and FIB Tomography,” *Journal of Nuclear Materials,* vol. 504, pp. 144-160, 2018.

[11] K. Une, K. Sakamoto, M. Aomi, J. Matsunaga, Y. Etoh, I. Takagi, S. Miyamura, T. Kobayashi and K. Ito, “Hydrogen Absorption Mechanism of Zirconium Alloys Based on Characterization of Oxide Layer,” *Zirconium in the Nuclear Industry: 16th International Symposium,* vol. 8, no. 5, pp. 401-432, 2011.

[12] Y. R. Than, M. R. Wenman, B. D. C. Bell, S. R. Ortner, H. Swan and R. W. Grimes, “Modelling and experimental analysis of the effect of solute iron in thermally grown Zircaloy-4 oxides,” *Journal of Nuclear Materials,* vol. 509, pp. 114-123, 2018.

[13] Y. Hatano, M. Sugisaki, K. Kitano and M. Hayashi, “Role of intermetallic precipitates in

hydrogen transport through oxide films on Zircaloy," *Zirconium in the Nuclear Industry: Twelfth International Symposium,* pp. 901-917, 2000.

[14] T. Isobe, T. Murai and Y. Mae, "Anodic protection provided by precipitates in aqueous corrosion of Zircaloy," *Zirconium in the Nuclear Industry: Eleventh International Symposium,* vol. 1295, pp. 203-217, 1996.

[15] D. Charquet, R. Hahn, E. Ortlieb, J. P. Gros and J. F. Wadier, "Solubility limits and formation of intermetallic precipitates in ZrSnFeCr alloys," *Zirconium in the Nuclear Industry: Eighth International Symposium,* pp. 405-422, 1989.

[16] Y. Dong, A. T. Motta and E. A. Marquis, "Atom probe tomography study of alloying element distributions in Zr alloys and their oxides," *Journal of Nuclear Materials,* vol. 442, no. 1-3, pp. 270-281, 2013.

[17] G. Sundell, M. Thuvander and H.-O. Andrén, "Enrichment of Fe and Ni at metal and oxide grain boundaries in corroded Zircaloy-2," *Corrosion Science,* vol. 65, pp. 10-12, 2012.

[18] G. Sundell, M. Thuvander and H.-O. Andrén, "Tin clustering and precipitation in the oxide during autoclave corrosion of Zircaloy-2," *Journal of Nuclear Materials,* vol. 456, pp. 409-414, 2015.

[19] G. Sundell, M. Thuvander, P. Tejland, M. Dahlbäck, L. Hallstadius and H.-O. Andrén, "Redistribution of alloying elements in Zircaloy-2 after in-reactor exposure," *Journal of Nuclear Materials,* vol. 454, no. 1-3, pp. 178-185, 2014.

[20] S. Abolhassani, R. Restani and L. Hallstadius, "Comparative analysis of the evolution of Zircaloy-2 cladding irradiated in BWR," in *Top Fuel 2015- Reactor Fuel Performance*, 2015.

[21] A. Baris, S. Abolhassani, Y. L. Chiu and H. E. Evans, "Observation of Crack Microstructure in Oxides and its Correlation to Oxidation and Hydrogen-uptake by 3D FIB Tomography – Case of Zr-ZrO2 in reactor," *Materials at High Temperatures,* pp. 1-8, 2017.

[22] M. Dahlbäck, L. Hallstadius, M. Limbäck, G. Vesterlund, T. Andersson, P. Witt, J. Izquierdo, B. Remartinez, M. Diaz, J. L. Sacedon and A. M. Alvarez, "The Effect of Liner Component Iron Content on Cladding Corrosion, Hydriding, and PCI Resistance," *Journal of ASTM International,* vol. 2, no. 9, pp. 1-23, 2005.

[23] T. Andersson, T. Thorvaldsson, A. Wilson and A. M. Wardle, "Influence of Thermal Processing and Microstructure on the Corrosion Behaviour of Zicaloy-4 Tubing," in *IAEA Int. Symp. on Improvements in Water Reactor Fuel Technology and Utilization*, Stockholm, 1987.

[24] S. Abolhassani, D. Gavillet, F. Groeschel, P. Jourdain and H. U. Zwicky, "Recent observation on the evolution of the secondary phase particles in Zircaloy-2 under irradiation in a BWR up to a high burn-up," in *International Topical Meeting; LWR Fuel Performance meeting*, Park City, USA, pp. 470-484, 2000.

[25] S. Abolhassani, S. Bart, J. Bertsch, M. Grosse, L. Hallstadius, A. Hermann, G. Kuri, G. Ledergerber, C. Lemaignan, M. Martin, S. Portier, C. Proff, R. Restani, S. Valance, S. Valizadeh and H. Wiese, "Corrosion and Hydrogen Uptake in Zirconium Claddings Irradiated in Light Water Reactors," in *Zirconium in the Nuclear Industry: 17th International Symposium*, 2015, pp. 540-573.

[26] A. Hermann, H. Wiese, R. Bühner, M. Steinemann and G. Bart, "Hydrogen Distribution Between Fuel Cladding Metal and Overlying Corrosion Layers," in *Proceedings of the ANS International Topical Meeting on LWR Fuel Performance*, Park City, Utah, American Nuclear Society, LaGrange Park, IL, 2000.

[27] G. Ledergerber, S. Valizadeh, J. Wright, M. Limbäck, L. Hallstadius, D. Gavillet, S. Abolhassani, F. Nagase, T. Sugiyama, W. Wiesenack and T. Tverberg, "Fuel performance beyond design - Exploring the limits," in *LWR Fuel Performance Meeting/Top Fuel/WRFPM 2010*, Orlando, FL, 2010.

[28] S. Abolhassani, M. Dadras, M. Leboeuf and D. Gavillet, “In situ study of the oxidation of Zircaloy-4 by ESEM,” *Journal of nuclear materials,* vol. 321, no. 1, pp. 70-77, 2003.

[29] K. Takeda and H. Anada, “Mechanism of corrosion rate degradation due to tin,” in *Zirconium in the Nuclear Industry: Twelfth International Symposium*, ASTM International, 2010, pp. 592-608.

[30] D. Khatamian and F. D. Manchester, “An ion beam study of hydrogen diffusion in oxides of Zr and Zr-Nb (2.5 wt%): I. Diffusion parameters for dense oxide,” *Journal of Nuclear Materials,* vol. 166, no. 3, pp. 300-306, 1989.